Topological Triply Degenerate Points Induced by Spin-Tensor-Momentum Couplings

Haiping Hu, Junpeng Hou, Fan Zhang, and Chuanwei Zhang*
Department of Physics, The University of Texas at Dallas, Richardson, Texas 75080, USA

(Received 30 September 2017; published 12 June 2018)

The recent discovery of triply degenerate points (TDPs) in topological materials has opened a new perspective toward the realization of novel quasiparticles without counterparts in quantum field theory. The emergence of such protected nodes is often attributed to spin-vector-momentum couplings. We show that the interplay between spin-tensor- and spin-vector-momentum couplings can induce three types of TDPs, classified by different monopole charges ($\mathcal{C} = \pm 2, \pm 1, 0$). A Zeeman field can lift them into Weyl points with distinct numbers and charges. Different TDPs of the same type are connected by intriguing Fermi arcs at surfaces, and transitions between different types are accompanied by level crossings along high-symmetry lines. We further propose an experimental scheme to realize such TDPs in cold-atom optical lattices. Our results provide a framework for studying spin-tensor-momentum coupling-induced TDPs and other exotic quasiparticles.

DOI: 10.1103/PhysRevLett.120.240401

Introduction.—Topological states of matter [1,2] provide a fertile ground for discovering new quasiparticles in condensed matter physics, such as Weyl [3–19] and Dirac fermions [19–25], which were originally predicted in high-energy physics and recently observed in solid-state materials [26]. In topological semimetals, Weyl and Dirac points correspond to two- and fourfold degenerate linear band crossing points, hallmarks of relativistic particles with half-integer spins. Remarkably, the recent discovery of triply degenerate points (TDPs) [27–39] in semimetals has opened an avenue for exploring new types of quasiparticles that have no analog in quantum field theory. Such TDPs possess effective integer spins while preserving Fermi statistics and linear dispersions.

Generally, the linearly dispersed quasiparticles near band degeneracies can be described by Hamiltonians with a spin-vector-momentum coupling $\sim \boldsymbol{k} \cdot \boldsymbol{F}$, where $\boldsymbol{F} = (F_x, F_y, F_z)$ is a spin vector. A degenerate point acts like a magnetic monopole in momentum space with a topological charge $\mathcal{C}$ determined by the quantized Berry flux emanating from the point. In this context, a TDP with $F = 1$ behaves like a three-component fermion with $\mathcal{C} = \pm 2$. However, it is well known that a full description of any large spin with $F \geq 1$ naturally involves spin tensors up to rank $2F$. For instance, there exist six rank-2 spin quadrupole tensors $N_{ij} = (F_i F_j + F_j F_i)/2 - \delta_{ij} \boldsymbol{F}^2/3$ for $F = 1$, in addition to the three vector components F_i $(i = x, y, z)$. Therefore, two questions naturally arise. Can spin-tensor-momentum couplings produce novel types of TDPs with distinct topological properties? If so, how can such novel TDPs and associated spin-momentum couplings be realized in realistic systems?

In this Letter, we address these two important questions by showing that two novel types of TDPs can emerge from the interplay between spin-vector- and spin-tensor-momentum couplings, and cold-atom optical lattices provide an attractive platform for their realizations. We call the TDPs described by the spin-vector-momentum coupling type I [27–39] and the TDPs induced by spin-tensor-momentum couplings types II and III. Here are our main results. First, the three types have different topological charges: $\mathcal{C} = \pm 2$, ± 1, and 0 for types I, II, and III, respectively. A Zeeman field can lift them into Weyl points with distinct numbers and charges.

Second, the topological transitions between different types, accompanied by level crossings along high-symmetry lines, can be achieved by tuning the relative strengths of spin-vector- and spin-tensor-momentum couplings. By constructing a minimum three-band lattice model, we display different types of TDPs in the bulk and their exotic Fermi arcs at the surface.

Third, since the type-II and type-III TDPs have not been discovered before, we propose the first experimental scheme for realizing type II and required spin-momentum couplings using cold atoms in an optical lattice. Spin-vector-momentum coupling is crucial for many important condensed matter phenomena, and its recent experimental realization in ultracold atomic gases [40–51] has provided a highly controllable and disorder-free platform for exploring topological quantum matter. In cold atoms, spins are modeled by atomic hyperfine states, and a spin with $F \geq 1$ can be naturally obtained. By now, various types of spin-vector-momentum coupling for both spin 1/2 and spin 1 have been proposed and realized [40–54]. A scheme for realizing a spin-tensor-momentum coupling of spin-1 atoms has also been proposed recently [55], with ongoing experimental efforts [56]. Our scheme is built on these experimentally available setups [50,53] and may even pave

the way for identifying solid-state materials with our novel types of TDPs.

Triply degenerate points.—As a direct extension of a twofold degenerate Weyl point described by $H = \boldsymbol{k}\cdot\boldsymbol{\sigma}$, the simplest TDP should be described by $H = \boldsymbol{k}\cdot\boldsymbol{F}$, with the spin-1 vector $\boldsymbol{F}$ [27–39]. The band structure around such a TDP is shown in Fig. 1(a), with a flat band located at the center and linear dispersions along all directions for the three bands. We label the band indices n for the lower, middle, and upper bands as -1, 0, and 1, respectively. The corresponding wave function for band n is denoted as $|\psi_n(\boldsymbol{k})\rangle$. The topological property of the TDP can be characterized by the first Chern numbers

$$\mathcal{C}_n = \frac{1}{2\pi}\oint_S \boldsymbol{\Omega}_n(\boldsymbol{k})\cdot d\boldsymbol{S}, \tag{1}$$

where $\boldsymbol{S}$ is a closed surface enclosing the TDP and $\boldsymbol{\Omega}_n(\boldsymbol{k}) = \boldsymbol{\nabla}_{\boldsymbol{k}}\times\langle\psi_n(\boldsymbol{k})|i\boldsymbol{\nabla}_{\boldsymbol{k}}|\psi_n(\boldsymbol{k})\rangle$ is the Berry curvature of band n. For $H = \boldsymbol{k}\cdot\boldsymbol{F}$, $\boldsymbol{\Omega}_n(\boldsymbol{k}) = -n\boldsymbol{k}/k^3$, yielding $\mathcal{C}_n = -2n$ for the three bands. The monopole charge $\mathcal{C}$ can be defined as the Chern number of the lower band, i.e., $\mathcal{C} = \mathcal{C}_{-1}$. Thus, this simplest TDP has $\mathcal{C} = 2$ and behaves as a momentum-space monopole carrying two monopole charges.

Novel types of TDPs can emerge when spin-tensors are also considered. Since a constant spin-tensor perturbation $\sim N_{ij}$ would break the threefold degeneracy of $H = \boldsymbol{k}\cdot\boldsymbol{F}$, the stabilization of novel TDPs with linear dispersions requires the coupling of spin tensors with momentum. For general linear Hamiltonians with $H(\boldsymbol{k}) = -H(-\boldsymbol{k})$, the property $\boldsymbol{\Omega}_n(\boldsymbol{k}) = \boldsymbol{\Omega}_{-n}(-\boldsymbol{k})$ dictates $\mathcal{C}_{+1} = -\mathcal{C}_{-1}$ for the upper and lower bands, and $\mathcal{C}_0 = 0$ for the middle one. Moreover, it can be proved that $|\mathcal{C}_n| \le 2$ for such linear Hamiltonians [58]. Therefore, the monopole charges for TDPs can only be ±2, ±1, and 0, indicating that all possible TDPs can be classified into three types: type I with $\mathcal{C} = \pm2$, type II with $\mathcal{C} = \pm1$, and type III with $\mathcal{C} = 0$.

All three types of TDPs can be illustrated using the following simple model [58]:

$$H(\boldsymbol{k}) = k_xF_x + k_yF_y + k_z(\alpha F_z + \beta N_{ij}), \tag{2}$$

where the spin tensor N_{ij} is coupled to k_z. By choosing different types of spin tensors and tuning the relative strength of the spin-tensor-momentum coupling β/α, we find that (i) the three spin tensors N_{xx}, N_{yy}, and N_{xy} do not change the monopole charge $\mathcal{C} = \pm2$ of the type-I TDP, (ii) the tensor N_{zz} induces a $\mathcal{C} = \pm1$ TDP for $|\beta| > |\alpha| \neq 0$, dubbed type II and depicted in Fig. 1(b), and (iii) the tensor N_{xz} or N_{yz} induces a $\mathcal{C} = 0$ TDP for $|\beta| > 2|\alpha| \neq 0$, dubbed type III and depicted in Fig. 1(c). Markedly, the energy dispersions are linear around all three types of TDPs.

Type-II TDPs.—Type-II TDPs can be induced from the type-I ones by choosing N_{ij} as $F_z^2 = N_{zz} + \frac{2}{3}$ in Eq. (2). Since the additional spin-independent term $2\beta k_z/3$ does not affect the eigenstates or any topological transition, we use F_z^2 instead of N_{zz} for a better presentation of our results. To study the transition between type-I and type-II TDPs due to the competition between spin-vector- and spin-tensor-momentum couplings, we fix $\beta = 1$, vary α, and calculate $\mathcal{C}_n$ numerically using Eq. (1). As exhibited in Fig. 2(a), the lower-band Chern number $\mathcal{C}_{-1}$ (the monopole charge) changes from 2 (type I) to ±1 (type II), and then to -2 (type I) with decreasing values of α.

The topological transitions can be understood by the band crossings [58] along the $k_x = k_y = 0$ line, as sketched in Figs. 2(b)–2(e). Note that the Chern number of each band has two contributions from the $k_z < 0$ and $k_z > 0$ branches

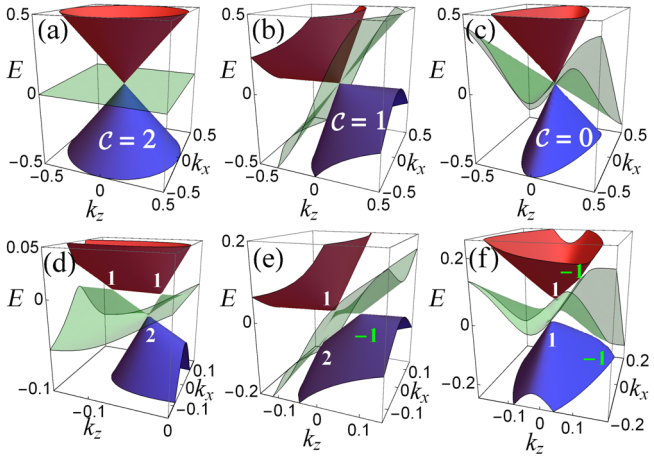

FIG. 1. (a)–(c) Band structures of three types of TDPs in the $k_y = 0$ plane for model (2). (a) Type I with $\alpha = 1$ and $\beta = 0$. (b) Type II with $\alpha = 1$, $\beta = 2$, and N_{ij} is chosen as F_z^2. (c) Type III with $\alpha = 1$, $\beta = 3$, and $N_{ij} = N_{xz}$. (d)–(f) Splittings of three types of TDPs due to a Zeeman perturbation εF_z with $\varepsilon = 0.05$. (d) Type I splits into two linear Weyl points with $\mathcal{C} = 1$ and one double-Weyl point [57] with $\mathcal{C} = 2$; note that $\beta = 0.5$ is used instead of 0. (e) Type II splits into two linear Weyl points with $\mathcal{C} = \pm1$, and one double-Weyl point [57] with $\mathcal{C} = 2$. (f) Type III splits into four linear Weyl points with $\mathcal{C} = \pm1$.

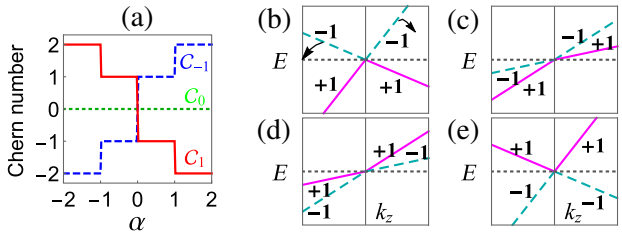

FIG. 2. Phase transitions between type-I and type-II TDPs by tuning α while fixing $\beta = 1$ in Eq. (2). (a) Chern numbers as functions of α for the lower (dashed blue), middle (dotted green), and upper (solid red) bands. (b)–(e) Band structures along the $k_x = k_y = 0$ line with $\alpha = 2$, 0.5, -0.5, and -2, respectively. We have labeled the Chern contributions of each branch: $+1$ (the solid magenta lines), -1 (the dashed cyan lines), and 0 (the dotted black lines).

in the surface integral of Eq. (1): $\mathcal{C} = \mathcal{C}_{k_z<0} + \mathcal{C}_{k_z>0}$. When $\alpha > 1$, the spin-vector-momentum coupling $k_z F_z$ dominates and model (2) is adiabatically connected to $H = \boldsymbol{k} \cdot \boldsymbol{F}$ (type I with $\mathcal{C} = 2$); the contributions from the two branches of the lower band are $\mathcal{C}_{k_z<0} = \mathcal{C}_{k_z>0} = +1$, as shown in Fig. 2(b). With decreasing values of α, the $k_z < 0$ ($k_z > 0$) branch of the lower band rotates clockwise (counterclockwise) in the $E - k_z$ plane. At $\alpha = 1$, the middle band crosses simultaneously with the $k_z < 0$ branch of the upper band, and the $k_z > 0$ branch of the lower band. After the band crossing, as shown in Fig. 2(c), the lower band consists of two branches, with Chern contributions $\mathcal{C}_{k_z<0} = 1$ and $\mathcal{C}_{k_z>0} = 0$, yielding a type-II TDP with $\mathcal{C} = 1$, which is consistent with the numerical results. With further decreasing α values, another level crossing occurs between the middle band and the $k_z < 0$ ($k_z > 0$) branch of the lower (upper) band at $\alpha = 0$, as shown in Fig. 2(d). This crossing changes $\mathcal{C}$ from 1 to -1, and the resulting TDP is still type II. A third band crossing occurs at $\alpha = -1$. For $\alpha < -1$, all bands are totally reversed compared to the $\alpha > 1$ case, as shown in Fig. 2(e), and the TDP is of type I, with $\mathcal{C} = -2$.

Type-I and type-II TDPs can be broken into different twofold degenerate Weyl points in the presence of perturbations. With an additional Zeeman term εF_z ($\varepsilon \ll 1$) to Eq. (2), the eigenspectrum of the total Hamiltonian shows that both types of TDPs are broken into three nodal points located at $W_\pm = (0, 0, -\varepsilon/(\alpha \pm \beta))$ and $W_3 = (0, 0, -\varepsilon/\alpha)$ [58], as illustrated in Figs. 1(d) and 1(e). The first two at $W_\pm$ are linear Weyl points, which have the same charge $\mathcal{C} = 1$ for type I ($|\beta| < |\alpha|$), but opposite charges $\mathcal{C} = \pm 1$ for type II ($|\beta| > |\alpha|$) [58]. The third node at W_3 is a multi-Weyl point [57] with $\mathcal{C} = 2$, whose dispersion is linear in the k_z direction but quadratic along the other two directions due to the indirect couplings between the lower and upper bands by F_x and F_y.

Splittings of TDPs can be understood using Fig. 2 with the small Zeeman field effectively lifting the middle band. For type I in Fig. 2(b), the horizontal band would cross the two branches with the same Chern contributions, resulting in two linear Weyl points of the same monopole charge. Apart from the two linear Weyl points, there still exists a twofold degenerate point with $\mathcal{C} = 2$. By contrast, type II in Fig. 2(c) has a different configuration of energy levels, and the horizontal band would cross the two branches with opposite Chern contributions, leading to two linear Weyl points carrying opposite charges.

Surface Fermi arcs.—For a 3D Weyl semimetal, it is well known that a Fermi arc exists in the 2D surface Brillouin zone connecting two projected Weyl points with opposite charges [5]. In the above discussions, we have seen that there exist TDPs of opposite charges for both type I and type II. Therefore, it is important to examine and compare their surface consequences. The coexistence of TDPs with opposite charges can be best illustrated by the following minimal model on a cubic lattice:

$$H(\boldsymbol{k}) = F_x \sin k_x + F_y \sin k_y + t_0(F_z + \beta F_z^2) \times (\cos k_x + \cos k_y + \cos k_z - 2 + \gamma), \quad (3)$$

which hosts two TDPs at $\boldsymbol{k} = (0, 0, \pm \arccos(-\gamma))$ for $|\gamma| < 1$. As displayed in Figs. 3(a) and 3(b), the band structure of model (3) with $\gamma = -0.5$ features two TDPs at $(0, 0, \pm\pi/3)$. Around the two TDPs, the Hamiltonians can be expanded as $H_\pm(\delta\boldsymbol{k}) = \delta k_x F_x + \delta k_y F_y \mp (\sqrt{3}t_0/2)\delta k_z(F_z + \beta F_z^2)$ to the linear order. The above effective Hamiltonian has the standard form of model (2), and the higher-order corrections would not affect the topological properties. Therefore, the two TDPs belong to type I for $|\beta| < 1$ and type II for $|\beta| > 1$.

To reveal and compare the surface hallmarks of the two types of TDPs, we impose a semi-infinite geometry with a (110) surface in our calculation. The surface Brillouin zone is expanded by (k_-, k_z) with $k_- = (k_x - k_y)/\sqrt{2}$. Since the middle band occupies most of the surface Brillouin zone at zero energy, we calculate the surface spectral density $A(\omega, \boldsymbol{k}) = \mathrm{Im}G(i\omega, \boldsymbol{k})/\pi$ [27] at a finite ω in order to distinguish the surface and bulk states. Here, $G = (i\omega - H)^{-1}$ is the single-particle Green's function. For type I, there are a pair of Fermi arcs, and each emanates from one projected TDP and ends at the other, as illustrated in Fig. 3(c). This clearly demonstrates the double monopole charges of type-I TDPs. For type II, the two projected TDPs are connected by only one Fermi arc, as depicted in

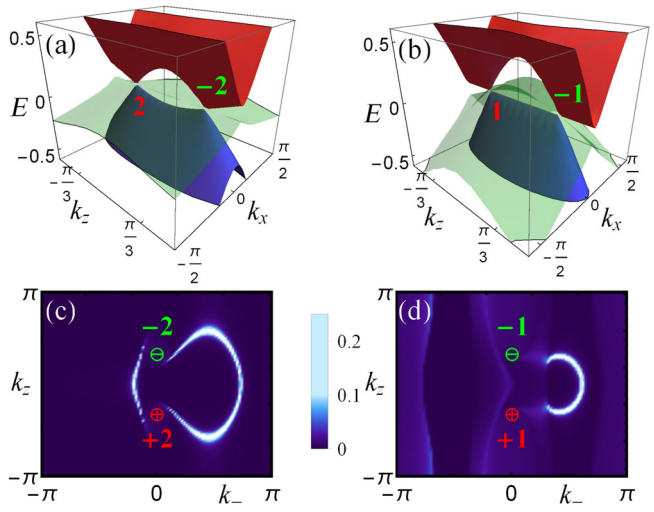

FIG. 3. Bulk band structures with TDPs and (110) surface spectral densities with Fermi arcs of model (3). (a),(c) Type I with $\mathcal{C} = \pm 2$ and two surface arcs. (b),(d) Type II with $\mathcal{C} = \pm 1$ and only one surface arc. In both cases, two TDPs appear at $(0, 0, \pm\pi/3)$, and each projected node is marked by its monopole charge. In our calculation, $\gamma = -0.5$, $\omega = 0.25$, and $t_0 = 0.5$ are used; $\beta = 0.5$ is used in (a) and (c), and $\beta = 1.5$ in (b) and (d).

Fig. 3(d). This agrees well with the single monopole charges of type-II TDPs.

Type-III TDPs.—The spin tensor N_{xz} or N_{yz} in model (2) can induce the topological transition of a TDP from type I to type III. Here, we use $N_{ij} = N_{xz}$ and $\alpha = 1$ to illustrate the transition [58]. The TDP is of type I for $|\beta| < 2$ and type III for $|\beta| > 2$. At $|\beta| = 2$, the bands cross along two lines $k_z \pm k_x = k_y = 0$, as shown in Fig. 4(b). At one of these two line nodes, e.g., $k_z - k_x = k_y = 0$, the band energies are found to be $-\beta k_z/2$ and $(\beta \pm \sqrt{32+\beta^2})k_z/4$. Clearly, at $\beta = 2$ the upper (lower) and middle bands cross at the $k_z < 0$ ($k_z > 0$) branch. The band crossing of the other line node is rather similar. Because each band crossing changes the Chern number by 1 and the crossings along the two lines are in the same branch, the Chern number must be changed by 2, as shown in Fig. 4(a), yielding a transition of the TDP from type I with $\mathcal{C} = \pm 2$ to type III with $\mathcal{C} = 0$.

Although a type-III TDP has vanishing Chern numbers, it can exhibit nontrivial topological properties after breaking into linear Weyl points [58] in the presence of a small Zeeman field, as depicted in Fig. 1(f). There exist four Weyl points with $\mathcal{C} = \pm 1$ located at $(k_x, k_z) = (\pm\beta\varepsilon/(\beta - 2\alpha), 2\varepsilon/(\beta - 2\alpha))$ and $(\pm\beta\varepsilon/(\beta + 2\alpha), -2\varepsilon/(\beta + 2\alpha))$ in the $k_y = 0$ plane. From the above discussions, we can see that the three types of TDPs have different patterns of Weyl points after splitting, which results in distinct surface states since the surface Fermi arcs can connect only two Weyl points of opposite charges. Therefore, while for type I the Fermi arcs connect only Weyl points originating from different TDPs, for type II and type III there may exist Fermi arcs connecting the Weyl points originating from the same TDP. These features may be used to identify TDPs of different types.

Experimental realization and observation.—The type-II TDPs can be realized by coupling three atomic hyperfine states (e.g., the $6^2S_{1/2}$ ground-state manifold of a ^{133}Cs atom: $g_1 = |4, -4\rangle$, $g_0 = |3, -3\rangle$, and $g_{-1} = |4, -2\rangle$) using Raman beams in a spin-dependent square lattice [58]. The three states are used for mimicking the spin-1 degree of freedom, and the proposed scheme is based on techniques used in the recent experimental realization of 2D Rashba spin-orbit coupling for spin 1/2 in optical lattices [50]. The atom-light interactions include two crucial parts. One part is used for generating the spin-dependent square lattice potentials $V_{g_{\pm 1}} \propto [\sin(2k_0x) + \sin(2k_0y)]$ and $V_{g_0} \propto [-\sin(2k_0x) - \sin(2k_0y)]$ in the x-y plane with one laser beam [53]. In the tight-binding limit, the g_{+1} and g_{-1} components stay on the same lattice sites. The other part is used for inducing the required spin-momentum couplings between the three hyperfine states, which can be achieved by adding another three Raman beams $\boldsymbol{E}_{R_1,R_3} = E_{R_1,R_3} e^{\mp i k_m z}[\hat{\boldsymbol{x}}\cos(2k_0y) \mp \hat{\boldsymbol{y}}\cos(2k_0x)]$ and $\boldsymbol{E}_{R_2} = E_{R_2} e^{ik_1 z}(i\hat{\boldsymbol{x}} + \hat{\boldsymbol{y}})$. The resulting Raman couplings between $g_{\pm 1}$ and g_0 are $M_{\pm 1,0} \propto e^{i(k_1 \pm k_m)z}[\cos(2k_0x) \pm i\cos(2k_0y)]$ [50,58]. Because the spatially dependent phase factors contain both spin-vector and spin-tensor components, they would produce both spin-vector- and spin-tensor-momentum couplings $\sim k_z(k_1F_z^2 + k_mF_z)$ in a chosen gauge. A careful analysis of the tight-binding model on the square lattice shows that the band structure contains two TDPs, located at (0,0) and $(\pi, 0)$ in the k_x-k_y plane at a constant k_z, similar to the case of model (3). Around these TDPs, the effective Hamiltonians have the standard form of Eq. (2), with the emergence of spin-tensor-momentum coupling. Type-II TDPs require $|k_1| > |k_m|$, which is naturally realized here since $k_1 \approx \sqrt{k_m^2 + 4k_0^2}$ in our scheme [58].

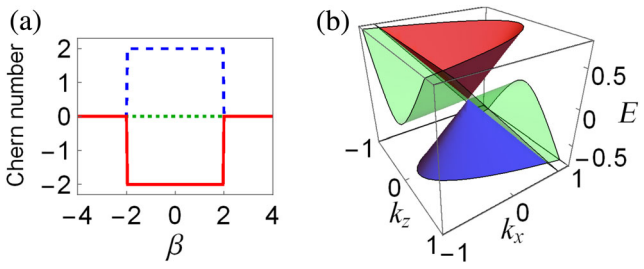

FIG. 4. Phase transitions between type-I and type-III TDPs by tuning β while fixing $\alpha = 1$ in Eq. (2). (a) Chern numbers as functions of β for the lower (dashed blue), middle (dotted green), and upper (solid red) bands. (b) Band crossing at the two transition lines with $\beta = 2$.

The linear band dispersions and the threefold degeneracy of a TDP may be detected experimentally using the momentum-resolved radio-frequency spectroscopy [66], as demonstrated in recent experiments for 2D spin-orbit coupled atomic gases through spin-injection methods [45–48]. Moreover, when the atomic gas is confined to a hard wall box potential similar to those realized in recent experiments [67,68], surface Fermi arcs would emerge at the boundary, which may also be observed using momentum-resolved radio-frequency spectroscopy.

Discussions.—We have proposed and demonstrated that the interplay between spin-vector- and spin-tensor-momentum couplings can induce two novel types of TDPs possessing distinct topological properties (e.g., Chern numbers, breaking into Weyl points, surface Fermi arcs, etc.) from the already discovered type-I TDP in solid-state materials. In particular, our proposed spin-tensor-momentum coupling mechanism should open a broad avenue for exploring novel topological quantum matter, and our results have already showcased two prime examples, i.e., the type-II and type-III TDPs.

Our results may motivate further theoretical and experimental studies of TDPs and other novel topological matter. Although our proposed experimental scheme is for cold-atom optical lattices, similar type-II and type-III TDPs may also be found in some solid-state materials in certain space

groups by first-principles calculations [69] and angle-resolved photoemission spectroscopy experiments. Moreover, we note that a type-I TDP has recently been experimentally realized in the parameter space of a superconducting qutrit [70], where the type-II and type-III TDPs may also be realized similarly. Finally, although we focus on the spin-1 rank-2 tensors for the purpose of studying TDPs, there exist higher-rank spin-tensors for higher spin systems, whose couplings with momentum may give rise to nontrivial topological matter with unprecedented properties.

This work is supported by the National Science Foundation (NSF) (Grant No. PHY-1505496), Army Research Office (ARO) (Grant No. W911NF-17-1-0128), Air Force Office of Scientific Research (AFOSR) (Grant No. FA9550-16-1-0387), and UTD Research Enhancement Funds.

*chuanwei.zhang@utdallas.edu

[1] M. Z. Hasan and C. L. Kane, Colloquium: Topological insulators, Rev. Mod. Phys. **82**, 3045 (2010).
[2] X.-L. Qi and S.-C. Zhang, Topological insulators and superconductors, Rev. Mod. Phys. **83**, 1057 (2011).
[3] G. Volovik, *The Universe in a Helium Droplet* (Oxford University Press, Oxford, 2003).
[4] S. Murakami, Phase transition between the quantum spin Hall and insulator phases in 3D: Emergence of a topological gapless phase, New J. Phys. **9**, 356 (2007).
[5] X. G. Wan, A. M. Turner, A. Vishwanath, and S. Y. Savrasov, Topological semimetal and Fermi-arc surface states in the electronic structure of pyrochlore iridates, Phys. Rev. B **83**, 205101 (2011).
[6] A. A. Burkov and L. Balents, Weyl Semimetal in a Topological Insulator Multilayer, Phys. Rev. Lett. **107**, 127205 (2011).
[7] M. Hirschberger, S. Kushwaha, Z. Wang, Q. Gibson, S. Liang, C. A. Belvin, B. A. Bernevig, R. J. Cava, and N. P. Ong, The chiral anomaly and thermopower of Weyl fermions in the half-Heusler GdPtBi, Nat. Mater. **15**, 1161 (2016).
[8] S.-M. Huang *et al.*, A Weyl fermion semimetal with surface Fermi arcs in the transition metal monopnictide TaAs class, Nat. Commun. **6**, 7373 (2015).
[9] B. Q. Lv *et al.*, Experimental Discovery of Weyl Semimetal TaAs, Phys. Rev. X **5**, 031013 (2015).
[10] B. Q. Lv *et al.*, Observation of Weyl nodes in TaAs, Nat. Phys. **11**, 724 (2015).
[11] C. Shekhar *et al.*, Observation of chiral magneto-transport in RPtBi topological Heusler compounds, arXiv:1604.01641.
[12] H. M. Weng, C. Fang, Z. Fang, B. A. Bernevig, and X. Dai, Weyl Semimetal Phase in Noncentrosymmetric Transition-Metal Monophosphides, Phys. Rev. X **5**, 011029 (2015).
[13] S.-Y. Xu *et al.*, Discovery of a Weyl fermion state with Fermi arcs in niobium arsenide, Nat. Phys. **11**, 748 (2015).
[14] S.-Y. Xu *et al.*, Discovery of a Weyl fermion semimetal and topological Fermi arcs, Science **349**, 613 (2015).
[15] L. X. Yang *et al.*, Weyl semimetal phase in the non-centrosymmetric compound TaAs, Nat. Phys. **11**, 728 (2015).
[16] L. Lu, Z. Wang, D. Ye, L. Ran, L. Fu, J. D. Joannopoulos, and M. Soljačić, Experimental observation of Weyl points, Science **349**, 622 (2015).
[17] C.-C. Liu, J.-J. Zhou, Y. Yao, and F. Zhang, Weak Topological Insulators and Composite Weyl Semimetals: $\beta - Bi_4X_4$ ($X = Br, I$), Phys. Rev. Lett. **116**, 066801 (2016).
[18] A. Lau, K. Koepernik, J. van den Brink, and C. Ortix, Generic Coexistence of Fermi Arcs and Dirac Cones on the Surface of Time-Reversal Invariant Weyl Semimetals, Phys. Rev. Lett. **119**, 076801 (2017).
[19] S. A. Yang, H. Pan, and F. Zhang, Dirac and Weyl Superconductors in Three Dimensions, Phys. Rev. Lett. **113**, 046401 (2014).
[20] Z. K. Liu *et al.*, A stable three-dimensional topological Dirac semimetal Cd_3As_2, Nat. Mater. **13**, 677 (2014).
[21] J. A. Steinberg, S. M. Young, S. Zaheer, C. L. Kane, E. J. Mele, and A. M. Rappe, Bulk Dirac Points in Distorted Spinels, Phys. Rev. Lett. **112**, 036403 (2014).
[22] Z. J. Wang, Y. Sun, X.-Q Chen, C. Franchini, G. Xu, H. Weng, X. Dai, and Z. Fang, Dirac semimetal and topological phase transitions in A_3Bi (A = Na, K, Rb), Phys. Rev. B **85**, 195320 (2012).
[23] J. Xiong, S. K. Kushwaha, T. Liang, J. W. Krizan, M. Hirschberger, W. Wang, R. J. Cava, and N. P. Ong, Evidence for the chiral anomaly in the Dirac semimetal Na_3Bi, Science **350**, 413 (2015).
[24] S. M. Young, S. Zaheer, J. C. Y. Teo, C. L. Kane, E. J. Mele, and A. M. Rappe, Dirac Semimetal in Three Dimensions, Phys. Rev. Lett. **108**, 140405 (2012).
[25] Z. K. Liu *et al.*, Discovery of a three-dimensional topological dirac semimetal, Na_3Bi, Science **343**, 864 (2014).
[26] A. A. Burkov, Topological semimetals, Nat. Mater. **15**, 1145 (2016).
[27] B. Bradlyn, J. Cano, Z. Wang, M. G. Vergniory, C. Felser, R. J. Cava, and B. A. Bernevig, Beyond Dirac and Weyl fermions: Unconventional quasiparticles in conventional crystals, Science **353**, aaf5037 (2016).
[28] B. Q. Lv *et al.*, Observation of three-component fermions in the topological semimetal molybdenum phosphide, Nature (London) **546**, 627 (2017).
[29] H. Yang, J. Yu, S. S. P. Parkin, C. Felser, C.-X. Liu, and B. Yan, Prediction of Triple Point Fermions in Simple Half-Heusler Topological Insulators, Phys. Rev. Lett. **119**, 136401 (2017).
[30] G. W. Winkler, Q.-S. Wu, M. Troyer, P. Krogstrup, and A. A. Soluyanov, Topological Phases in $InAs_{1-x}Sb_x$: From Novel Topological Semimetal to Majorana Wire, Phys. Rev. Lett. **117**, 076403 (2016).
[31] H. M. Weng, C. Fang, Z. Fang, and X. Dai, Topological semimetals with triply degenerate nodal points in θ-phase tantalum nitride, Phys. Rev. B **93**, 241202(R) (2016).
[32] Z. M. Zhu, G. W. Winkler, Q. S. Wu, J. Li, and A. A. Soluyanov, Triple Point Topological Metals, Phys. Rev. X **6**, 031003 (2016).
[33] H. M. Weng, C. Fang, Z. Fang, and X. Dai, Coexistence of Weyl fermion and massless triply degenerate nodal points, Phys. Rev. B **94**, 165201 (2016).

[34] G. Q. Chang *et al.*, Nexus fermions in topological symmorphic crystalline metals, Sci. Rep. **7**, 1688 (2017).

[35] I. C. Fulga and A. Stern, Triple point fermions in a minimal symmorphic model, Phys. Rev. B **95**, 241116(R) (2017).

[36] G. Chang *et al.*, Unconventional Chiral Fermions and Large Topological Fermi Arcs in RhSi, Phys. Rev. Lett. **119**, 206401 (2017).

[37] C. Y. Zhong, Y. Chen, Z.-M. Yu, Y. Xie, H. Wang, S. A. Yang, and S. Zhang, Three-dimensional Pentagon Carbon with a genesis of emergent fermions, Nat. Commun. **8**, 15641 (2017).

[38] J. B. Yu, B. H. Yan, and C.-X. Liu, Model Hamiltonian and time reversal breaking topological phases of antiferromagnetic half-Heusler materials, Phys. Rev. B **95**, 235158 (2017).

[39] X. M. Zhang, Z.-M. Yu, X.-L. Sheng, H. Y. Yang, and S. A. Yang, Coexistence of four-band nodal rings and triply degenerate nodal points in centrosymmetric metal diborides, Phys. Rev. B **95**, 235116 (2017).

[40] Y.-J. Lin, K. Jiménez-García, and I. B. Spielman, Spin-orbit-coupled Bose-Einstein condensates, Nature (London) **471**, 83 (2011).

[41] Z. K. Fu, P. J. Wang, S. J. Chai, L. H. Huang, and J. Zhang, Bose-Einstein condensate in a light-induced vector gauge potential using 1064-nm optical-dipole-trap lasers, Phys. Rev. A **84**, 043609 (2011).

[42] J.-Y. Zhang *et al.*, Collective Dipole Oscillations of a Spin-Orbit Coupled Bose-Einstein Condensate, Phys. Rev. Lett. **109**, 115301 (2012).

[43] C. Qu, C. Hamner, M. Gong, C. Zhang, and P. Engels, Observation of *Zitterbewegung* in a spin-orbit coupled Bose-Einstein condensate, Phys. Rev. A **88**, 021604(R) (2013).

[44] A. J. Olson, S.-J. Wang, R. J. Niffenegger, C.-H. Li, C. H. Greene, and Y. P. Chen, Tunable Laudan-Zener transitions in a spin-orbit-coupled Bose-Einstein condensate, Phys. Rev. A **90**, 013616 (2014).

[45] P. Wang, Z.-Q. Yu, Z. Fu, J. Miao, L. Huang, S. Chai, H. Zhai, and J. Zhang, Spin-Orbit Coupled Degenerate Fermi Gases, Phys. Rev. Lett. **109**, 095301 (2012).

[46] L. W. Cheuk, A. T. Sommer, Z. Hadzibabic, T. Yefsah, W. S. Bakr, and M. W. Zwierlein, Spin-Injection Spectroscopy of a Spin-Orbit Coupled Fermi Gas, Phys. Rev. Lett. **109**, 095302 (2012).

[47] L. H. Huang, Z. Meng, P. Wang, P. Peng, S.-L. Zhang, L. Chen, D. Li, Q. Zhou, and J. Zhang, Experimental realization of two-dimensional synthetic spin-orbit coupling in ultracold Fermi gases, Nat. Phys. **12**, 540 (2016).

[48] Z. Meng, L. Huang, P. Peng, D. Li, L. Chen, Y. Xu, C. Zhang, P. Wang, and J. Zhang, Experimental Observation of a Topological Band Gap Opening in Ultracold Fermi Gases with Two-Dimensional Spin-Orbit Coupling, Phys. Rev. Lett. **117**, 235304 (2016).

[49] R. A. Williams, M. C. Beeler, L. J. LeBlanc, K. Jiménez-García, and I. B. Spielman, Raman-Induced Interactions in a Single-Component Fermi Gas Near an *s*-Wave Feshbach Resonance, Phys. Rev. Lett. **111**, 095301 (2013).

[50] Z. Wu, L. Zhang, W. Sun, X.-T. Xu, B.-Z. Wang, S.-C. Ji, Y. Deng, S. Chen, X.-J. Liu, and J.-W. Pan, Realization of two-dimensional spin-orbit coupling for Bose-Einstein condensates, Science **354**, 83 (2016).

[51] D. L. Campbell, R. M. Price, A. Putra, A. Valdés-Curiel, D. Trypogeorgos, and I. B. Spielman, Magnetic phases of spin-1 spin-orbit-coupled Bose gases, Nat. Commun. **7**, 10897 (2016).

[52] B. M. Anderson, G. Juzeliūnas, V. M. Galitski, and I. B. Spielman, Synthetic 3D Spin-Orbit Coupling, Phys. Rev. Lett. **108**, 235301 (2012).

[53] B.-Z. Wang, Y.-H. Lu, W. Sun, S. Chen, Y. Deng, and X.-J. Liu, Dirac-, Rashba-, and Weyl-type spin-orbit couplings: Toward experimental realization in ultracold atoms, Phys. Rev. A **97**, 011605(R) (2018).

[54] Y. Li, X. Zhou, and C. Wu, Three-dimensional quaternionic condensations, Hopf invariants, and skyrmion lattices with synthetic spin-orbit coupling, Phys. Rev. A **93**, 033628 (2016).

[55] X.-W. Luo, K. Sun, and C. Zhang, Spin-Tensor-Momentum-Coupled Bose-Einstein Condensates, Phys. Rev. Lett. **119**, 193001 (2017).

[56] P. Engels and J. Zhang (private communication).

[57] C. Fang, M. J. Gilbert, X. Dai, and B. A. Bernevig, Multi-Weyl Topological Semimetals Stabilized by Point Group Symmetry, Phys. Rev. Lett. **108**, 266802 (2012).

[58] See Supplemental Material at http://link.aps.org/supplemental/10.1103/PhysRevLett.120.240401, which includes Refs. [59–65], for further discussions on topological invariants, another model exhibiting TDPs, phase transitions, the splitting of TDPs, and our experimental scheme.

[59] E. Majorana, Atoms oriented in a variable magnetic field, Nuovo Cimento **9**, 43 (1932).

[60] J. Schwinger, in *Quantum Theory of Angular Momentum*, edited by L. C. Biendenharn and H. Van Dam (Academic Press, New York, 1965).

[61] J. H. Hannay, The Berry phase for spin in the Majorana representation, J. Phys. A **31**, L53 (1998).

[62] P. Bruno, Quantum Geometric Phase in Majorana Stellar Representation: Mapping onto a Many-Body Aharonov-Bohm Phase, Phys. Rev. Lett. **108**, 240402 (2012); Q. Niu, Viewpoint: A quantum constellation, Physics **5**, 65 (2012).

[63] H. D. Liu and L. B. Fu, Representation of Berry Phase by the Trajectories of Majorana Stars, Phys. Rev. Lett. **113**, 240403 (2014).

[64] R. Barnett, D. Podolsky, and G. Refael, Geometrical approach to hydrodynamics and low-energy excitations of spinor condensates, Phys. Rev. B **80**, 024420 (2009).

[65] B. A. Bernevig and T. L. Hughes, *Topological Insulators and Topological Superconductors* (Princeton University, Princeton, NJ, 2013).

[66] J. T. Stewart, J. P. Gaebler, and D. S. Jin, Using photoemission spectroscopy to probe a strongly interacting Fermi gas, Nature (London) **454**, 744 (2008).

[67] A. L. Gaunt, T. F. Schmidutz, I. Gotlibovych, R. P. Smith, and Z. Hadzibabic, Bose-Einstein Condensation of Atoms in a Uniform Potential, Phys. Rev. Lett. **110**, 200406 (2013).

[68] B. Mukherjee, Z. Yan, P. B. Patel, Z. Hadzibabic, T. Yefsah, J. Struck, and M. W. Zwierlein, Homogeneous Atomic Fermi Gases, Phys. Rev. Lett. **118**, 123401 (2017).

[69] H. M. Weng and B. Wieder (private communication).

[70] X. Tan, D.-W. Zhang, Q. Liu, G. Xue, H.-F. Yu, Y.-Q. Zhu, H. Yan, S.-L. Zhu, and Y. Yu, Topological Maxwell Metal Bands in a Superconducting Qutrit, Phys. Rev. Lett. **120**, 130503 (2018).